photonics

MDPI

Article

On-Chip Reconfigurable Three-Waveguide Coupling Mode Switches on Silica Platform

Minghui Zhou [1,2], Shengyuan Zhang [1], Yingzhi Ding [1], Guoyan Zeng [1] and Daming Zhang [1,*]

1 State Key Laboratory of Integrated Optoelectronics, JLU Region, College of Electronic Science and Engineering, Jilin University, 2699 Qianjin Street, Changchun 130012, China; zhoumh23@mails.jlu.edu.cn (M.Z.); shengyuan25@mails.jlu.edu.cn (S.Z.); dingyz22@mails.jlu.edu.cn (Y.D.); zenggy21@mails.jlu.edu.cn (G.Z.)

2 College of Transportation Information, Jilin Communications Polytechnic, 63 Diantai Street, Changchun 130012, China

* Correspondence: zhangdm@jlu.edu.cn

Abstract

Reconfigurable mode switches can provide more flexible and advanced data exchange functions for complex on-chip optical networks. A reconfigurable mode-selective optical switch based on adiabatic progressive three-waveguide coupling (TWC) is proposed. As a proof of concept, the switching of E_{00} (E_{20})/E_{10} (E_{30}) dual-mode channels was successfully implemented and demonstrated. At 1550 nm, the insertion losses for E_{00}/E_{10} and E_{20}/E_{30} mode switches were lower than 7.86 and 10.76 dB, respectively. These values include the loss of the mode demultiplexer. The crosstalk was lower than −22.84 (−18.28) dB at 1550 nm. The switching rise time (10–90%) and fall time (10–90%) were 0.86 ms and 0.64 ms, respectively. On the silica platform, the scalability of the structural scheme was also verified, and the arbitrary selection and switching of the E_{00}, E_{10}, E_{20}, and E_{30} modes were achieved via the cascading of TWCs. The device can be used as an important component for the future large-scale integration and flexible switching of on-chip optical networks.

Keywords: silica PLC; mode switch; isothermal coupling; thermo-optic effect

1. Introduction

Data exchange is a key function of advanced optical networks. The integration of collaborative artificial intelligence into both industrial production and daily life has transformed traditional passive network transmission into a new, intelligent paradigm. This transformation significantly increases the demand for flexibility in data exchange. Developing multiple physical dimensions of light and utilizing spatial modes to simultaneously carry multiple optical signals can achieve the large-scale parallel processing of data transmission. In recent years, substantial efforts have been devoted to the development of multiplexing technologies, such as wavelength division multiplexing [1], polarization division multiplexing [2], and mode division multiplexing (MDM) [3]. Among these, MDM can be combined with other multiplexing techniques [4,5], emerging as one of the most effective approaches for enhancing communication capacity. Over the past years, a variety of passive components have been widely studied and demonstrated for MDM, such as mode multiplexers/demultiplexers, mode converters, multimode bends, mode switches, and multimode cross-connects [6–9].

Mode switching is regarded as a key component for realizing large-scale reconfigurable MDM networks. However, most existing approaches based on multimode interferometers,

Received: 8 December 2025
Revised: 6 January 2026
Accepted: 9 January 2026
Published: 12 January 2026

Y-junctions, Mach–Zehnder interferometers, and asymmetric directional couplers [10–13] can only enable data exchange between two or three modes, which is clearly insufficient to support higher-order mode optical communication networks. Multimode switching architectures based on micro-ring or micro-disk resonators [14,15] can achieve data switching among multiple modes and extend the number of supported channels, but their structural complexity and limited integrability hinder large-scale deployment. Therefore, to realize flexible on-chip interconnects for MDM, a major challenge lies in developing a simple and reconfigurable mode switch. The three-waveguide coupled (TWC) switch between the E_{00} mode and the E_{10} mode has been successfully verified and demonstrated on silicon-on-insulator and lithium niobate platforms [16–18] and arbitrary switching among the first three-order modes has been proposed [19], which is essential for future large-scale MDM systems. The SOI platform exhibits low switching power consumption and fast switching speeds due to its high thermo-optical coefficient and thermal conductivity. However, its high thermo-optical coefficient also results in elevated temperature sensitivity for WDM devices on this platform, preventing the realization of high-performance monolithic integrated WDM-MDM systems. Thin-film lithium niobate exhibits fast electro-optic switching speeds but suffers from poor inherent electro-optic stability, necessitating additional thermo-optic modulation to ensure stable switching rates. Silica platforms are a mature platform with a low transmission loss (0.12 dB/cm) [20], a low polarization-dependent loss (PDL), and a high coupling tolerance [21]. By using a 2% index contrast silica platform, the bend radius can be reduced to 1500 µm. Meanwhile, the silica platform features highly mature WDM devices, enabling the rapid realization of monolithic WDM-MDM systems. Power consumption in silica-based devices can be optimized to be as low as 20 mW through refined designs of isolation trenches and electrode geometries [22]. Our silica-based switch exhibits millisecond-level switching speeds (0.64–0.86 ms), which is sufficient for static reconfigurable MDM provisioning.

In this work, we design and experimentally demonstrate a TWC mode switch on a silica platform for E_{00} (E_{20})/E_{10} (E_{30}) modes. We further propose a non-crossing cascaded TWC architecture and successfully validate it experimentally, extending the design to the high-order E_{00}–E_{30} modes. From 1500 to 1630 nm, the insertion losses (ILs) of mode switching for E_{00}/E_{10} and E_{20}/E_{30} are lower than 8.07 dB and 14.52 dB, with −16.23 dB and −14.97 dB.

Meanwhile, the loss of the mode demultiplexer and coupling loss and the CT was lower than −22.84 (−18.28) dB. Furthermore, we optimize and expand the mode-selective switch for input E_{00} and output E_{00}–E_{30} in [19], reducing the number of beam splitters and achieving a non-crossing structure, which is experimentally verified. This facilitates the implementation of higher-order mode-selective switches.

2. Optical Design and Principles

As shown in Figure 1a, a reconfigurable and broadband adiabatic TWC mode switch was designed on a silica platform with a 2% index contrast. The operating wavelength was set to 1550 nm, corresponding to refractive index of 1.4737 for the core layer and 1.4448 for the cladding layer. The input combiner of the device adopts an adiabatic coupling design, whereas the combiner following the modulation arm adopts a TWC design. This three-waveguide coupling region (TWCR) consists of four TWC sections ($TWCR_{1–4}$), corresponding to mode selection among the E_{00}–E_{30} modes. Each TWC structure contains single-mode waveguides on both sides and a single-mode waveguide together with a multimode waveguide in the center. The bus waveguide is formed by connecting four waveguides of different widths using linear taper transitions. The two input ports and the output port of the multimode bus waveguide are defined as I_1, I_2, and O, respectively.

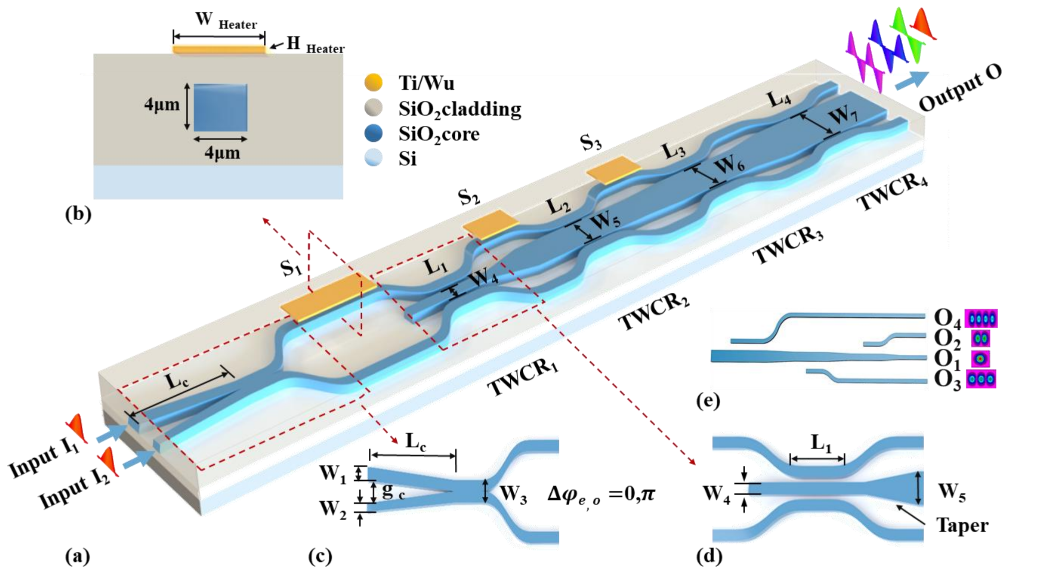

Figure 1. (**a**) Structural diagram of the device; (**b**) cross-section of upper arm waveguide on modulation arm; (**c**) adiabatic coupling; (**d**) three-waveguide coupling; (**e**) mode demultiplexers.

The adiabatic coupler at the input is designed based on the principle of mode evolution [19,20], and its structural parameters are shown in Figure 1c. The input waveguide widths, W_1 and W_2, taper linearly from 5 μm to 4 μm, with a coupling length L_c of 10,000 μm, while the gap g_c decreases from 12 μm to 0 μm, and eventually connects to a multimode output waveguide with a width W_3 of 8 μm at the end of the adiabatic transition. The subsequent Y-junction and the modulation arm waveguide are both single-mode waveguides with a height and width of 4 μm. The thermo-optic modulation of the silica waveguide by the Ti electrode with Au pads is adopted to implement the demanded phase; the electrode is 21 μm wide and 3000 μm long. The cross-section of the device's waveguide is shown in Figure 1b.

The modulation arm (s) behind the Y-branch only supports the E_{00} mode transmission. When the E_{00} mode is input from the wide waveguide port I_1, the light in the multimode output waveguide remains in the E_{00} mode, passing through the Y-branch then generating two E_{00} mode beams with identical phases and equal power. When input from the narrow waveguide port I_2, the light converts to the E_{10} mode in the multimode waveguide, and subsequent transmission through the Y-branch produces two E_{00} mode beams with opposite phases (phase difference of π) and equal optical power. This is critical to the operating state of the subsequent TWC system.

Based on the supermode theory [21,22], the TWCR was designed as shown in Figure 1d. A coupling structure consisting of two closely spaced single-mode waveguides can be regarded as an integrated system. When the input signal light enters from one of the waveguides, it will excite an even-symmetric mode SM_1 and an odd-symmetric mode SM_2 in this system, the initial phase of the two supermodes will be the same, the initial mode field integral will be the same as the mode field integral of the input light, and it can exist stably in the system due to the different propagation constants. When the mode field is superimposed, the signal light of the input waveguide (WG) will be all coupled into the adjacent waveguide, which needs to meet the two supermodes to transmit a distance along the *z*-axis direction to make the phase difference π. These supermodes can be mathematically expressed as

$$E(x,z) = e^{-j\beta_e z}\left(E_e(x) + E_o(x)e^{-j(\beta_o-\beta_e)z}\right) \tag{1}$$

where $E_e(E_o)$ is the electric field distribution of the even (odd) symmetric supermode and $\beta_e(\beta_o)$ is the corresponding propagation constant. Since the two supermodes possess different propagation constants, they can stably coexist. When the two supermodes propagate along the z-axis for a certain distance such that their phase difference reaches π, the initial modal field launched in one waveguide will be completely transferred to the adjacent waveguide, where the propagation distance satisfies, $z = \pi/(\beta_o - \beta_e)$.

We define this coupling distance as the beat length L_z. Based on $\beta = kn_{eff} = (2\pi/\lambda)n_{eff}$, (where k is the wave number in free space and n_{eff} is the effective refractive index) we obtain

$$L_Z = \frac{\pi}{\beta_o - \beta_e} = \frac{\lambda}{2(n_o - n_e)} \tag{2}$$

where λ is the wavelength of the input light, and n_o and n_e are the effective refractive indices of the odd-symmetric and even-symmetric modes in the system, respectively.

The supermode coupling composed of three single-mode waveguides is shown in Figure 2a,b. Two beams of incident signal light, with a phase difference $\Delta\varphi = 0$ and input from WG_1 and WG_3 at the same time, will excite an even-symmetric mode SM_1 and an odd-symmetric mode SM_2 and transmit a beat length L_z, and the signal light is all coupled from WG_1 and WG_3 into WG_2, as shown in Figure 2a. When $\Delta\varphi = \pi$, only an odd-symmetric mode SM_3 is excited in the system and transmits stably, without coupling, as shown in Figure 2b.

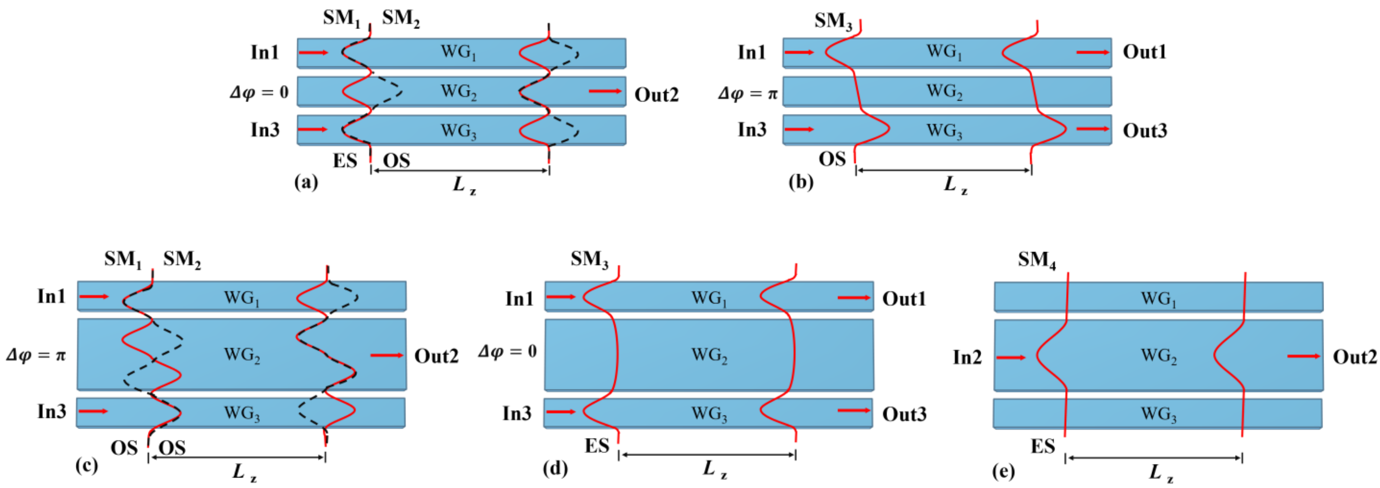

Figure 2. Supermode coupling characteristics and transmission behaviors in different waveguide coupling systems. (**a**,**b**) The excited supermode and transmission in the TWC systems of three single-mode waveguides: (**a**) corresponds to SM_1 and SM_2 (**b**) corresponds to SM_3; (**c**–**e**) The excited supermode and transmission in the TWC systems of two single-mode waveguides and one multimode waveguide supporting the E_{00} mode: (**c**) corresponds to SM_1, SM_2 (**d**) corresponds to SM_3 and (**e**) corresponds to SM_4.

The middle waveguide of TWCR is designed as a multimode waveguide supporting E_{00} mode transmission. As shown in Figure 2c–e, when two beams of signal light are incident from WG_1 and WG_3 with a phase difference $\Delta\varphi = \pi$, two odd-symmetric modes SM_1 and SM_2 are excited. After transmitting a coupling distance L_z, the signal light couples into WG_2, propagating as the E_{00} mode, as shown in Figure 2c. When the phase difference $\Delta\varphi = 0$, only the even-symmetric mode SM_3 is excited, which stably propagates in the system without coupling, as shown in Figure 2d. When the signal light is input from WG_2, only the even-symmetric mode SM_4 is excited, which stably propagates in the system without coupling, as shown in Figure 2e.

As shown in Figure 3, this is a TWC cascaded mode-selective system. When $n = 1$ ($n = 2$), this corresponds to the E_{00}/E_{10} (E_{20}/E_{30}) mode-selective structure. When the phase difference between the two incident beams of signal light in $TWCR_{2n-1}$ is 0 or 2π, the signal light will couple into the bus waveguide as even-symmetric modes, with the excited supermode and transmission characteristics as shown in Figure 2a. When the phase difference between the two incident beams of signal light in $TWCR_{2n}$ is π, the signal light will couple into the bus waveguide as odd-symmetric modes, as shown in Figure 2c. Here, the coupling conditions for $TWCR_{2n-1}$ and $TWCR_{2n}$ are equally applicable to the four-cascaded TWC structure.

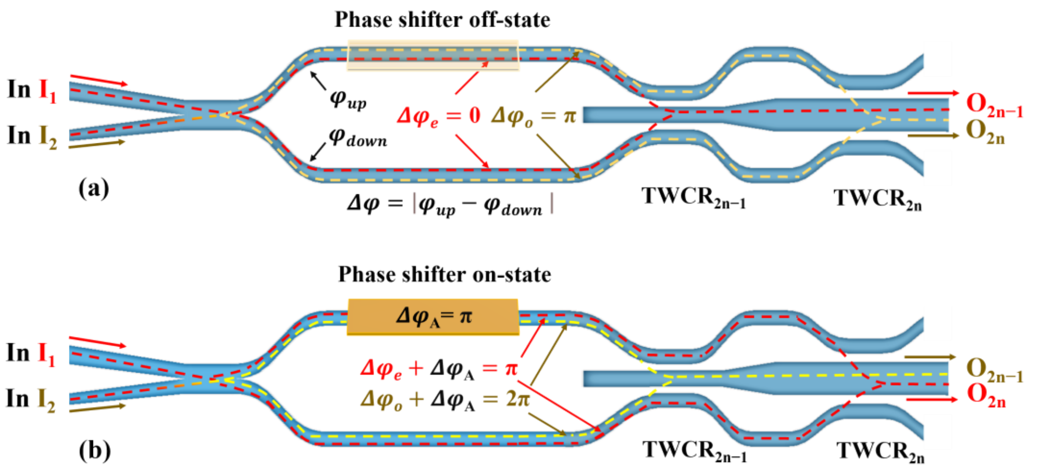

Figure 3. Schematic diagram of a TWC cascaded mode-selective system: (**a**) working process of selecting output mode in non-modulation; (**b**) working process of selecting output mode in modulation.

Then the signal light of E_{00} mode enters from port I_1 and the optical phase difference between the two modulation arms is $\Delta\varphi_e = 0$. In $TWCR_{2n-1}$, the two beams of signal light couple into the bus waveguide as the E_{00} mode, and the excited supermode and transmission characteristics are as shown in Figure 2a; in $TWCR_{2n}$, the signal light stably propagates without coupling as shown in Figure 2e, and the E_{00} mode is output finally. When the E_{00} mode enters from port I_2, the optical phase difference between the two modulation arms is $\Delta\varphi_o = \pi$. In $TWCR_{2n-1}$, the beams stably propagate without coupling as shown in Figure 2b; in $TWCR_{2n}$, the signal light couples into the bus waveguide and excites the E_{10} mode as shown in Figure 2c, and the E_{10} mode is output finally.

In summary, without modulation, this work can realize a two-mode-selective output by means of different input ports.

Figure 3b illustrates the operating mode of the structure with modulation. By applying a voltage to the electrode heater above the modulation arm waveguide, a modulation-induced phase difference $\Delta\varphi_A = 0$ is introduced into the light propagating through these modulation arm waveguides. When the E_{00} mode is launched through port I_1, the light in the upper modulation arm waveguide undergoes phase compensation—specifically, this varies the initial optical phase difference ($\Delta\varphi_e = 0$) between the two modulation arms to $\Delta\varphi_e = \pi$. Consequently, the E_{00} mode does not couple into the bus waveguide at $TWCR_{2n-1}$ and continues propagating to $TWCR_{2n}$, where it couples into the multimode bus waveguide and outputs as an odd-order mode. Similarly, when the E_{00} mode is launched through port I_2, the optical phase difference between the two modulation arms is adjusted from the initial $\Delta\varphi_o = \pi$ to $\Delta\varphi_e = 2\pi$. The two beams then couple at $TWCR_{2n-1}$ and enter the multimode bus waveguide as an even-order mode. This design enables mode-selective output through thermo-optic modulation, thereby eliminating the need for input port switching.

Based on the above working principle, the BPM was used to simulate and optimize the mode selectors for the E_{00}/E_{10} and E_{20}/E_{30} modes. Figure 4a–d present the simulated optical field distributions of the E_{00}/E_{10} mode-selective switch at 1550 nm with different operating conditions, whereas Figure 4e–h show those of the E_{20}/E_{30} mode-selective switch at 1550 nm with various operating conditions.

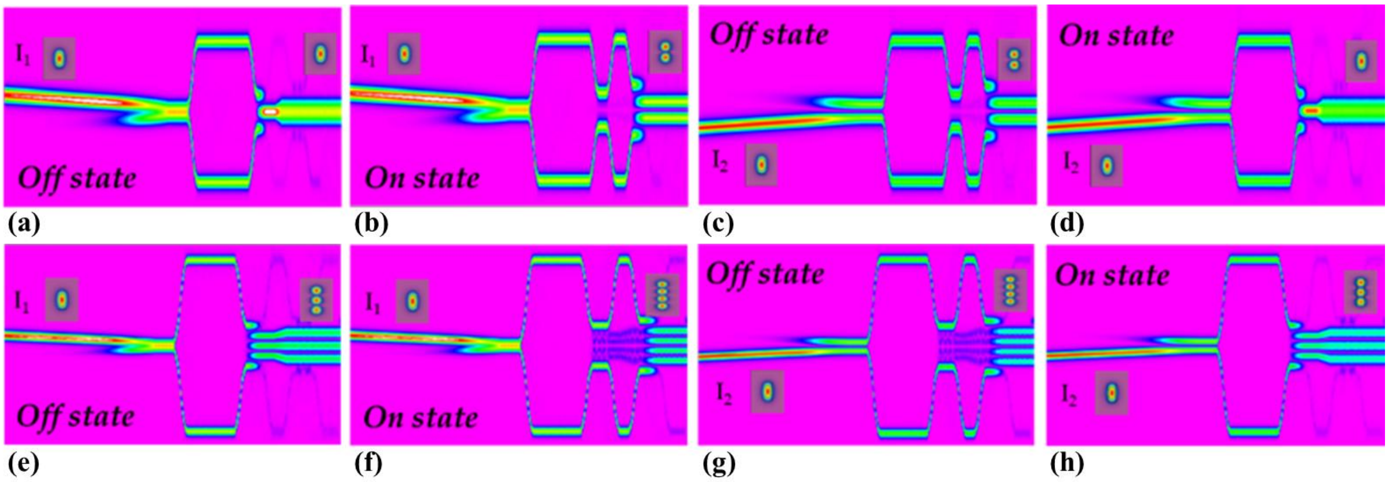

Figure 4. Optical field distributions of the E_{00}/E_{10} mode-selective switch: (**a**) I_1 in, E_{00} out, non-modulation; (**b**) I_1 in, E_{10} out, modulation; (**c**) I_2 in, E_{10} out, non-modulation; (**d**) I_2 in, E_{00} out, modulation; optical field distributions of the E_{20}/E_{30} mode-selective switch; (**e**) I_1 in, E_{20} out, non-modulation; (**f**) I_1 in, E_{30} out, modulation; (**g**) I_2 in, E_{30} out, non-modulation; (**h**) I_2 in, E_{20} out, modulation.

For the E_{00}/E_{10} mode-selective switch, the following observations were made: With the E_{00} mode input from port I_1, the output is E_{00} at $\Delta\varphi_A = 0$ (no modulation, Figure 4a) and E_{10} when the heating electrode is activated ($\Delta\varphi_A = \pi$, Figure 4b). From port I_2, the output switches to E_{10} at $\Delta\varphi_A = 0$ (Figure 4c) and reverts to E_{00} at $\Delta\varphi_A = \pi$ (Figure 4d). For the E_{20}/E_{30} mode-selective switch, the following observations were made: E_{00} input from port I_1 yields E_{20} at $\Delta\varphi_A = 0$ (Figure 4e) and E_{30} at $\Delta\varphi_A = \pi$ (heating electrode on, Figure 4f). From port I_2, E_{30} is output at $\Delta\varphi_A = 0$ (Figure 4g) and E_{20} at $\Delta\varphi_A = \pi$ (Figure 4h).

The simulation results are highly consistent with the theoretical analysis, confirming the excellent scalability and flexibility of the TWCR cascade structure when it is mode-selective.

To achieve conversion from the fundamental mode to higher-order modes, the effective refractive index of the high-order mode supported by the multimode bus waveguide must match that of the E_{00} mode in the single-mode waveguides on both sides of the system. Using the effective refractive index matching method [19] and taking the effective refractive index of the fundamental mode in a 4 μm wide silica waveguide as a reference, the widths of the multimode waveguides corresponding to the E_{10}, E_{20}, and E_{30} modes were determined. Specific structural parameters including the widths ($W_{4–7}$) and coupling lengths ($L_{1–4}$) of the relevant waveguides and coupling segments are summarized in Table 1.

Table 1. Structural parameters of TWCRs in the E_{00}/E_{10} and E_{20}/E_{30} mode-selective switches.

Mode-Selective Switch	E_{00}	E_{10}	E_{20}	E_{30}
$W_{4–7}$	3 μm	9.71 μm	15.56 μm	21.3 μm
$L_{1–4}$	435 μm	659 μm	917 μm	1140 μm

We simulated the spectra with different fabricated errors for the E_{00}/E_{10} mode-selective switch in Figure 5. When the waveguide width shifts −0.2 μm, the loss in

E_{00} mode increases to 0.5 dB and the loss in E_{10} mode increases to 1.2 dB. When the waveguide width shifts 0.2 μm, the loss in E_{20} mode is lower than 1 dB. When the waveguide width shifts 0.1 μm, the loss in E_{30} mode is lower than 1 dB.

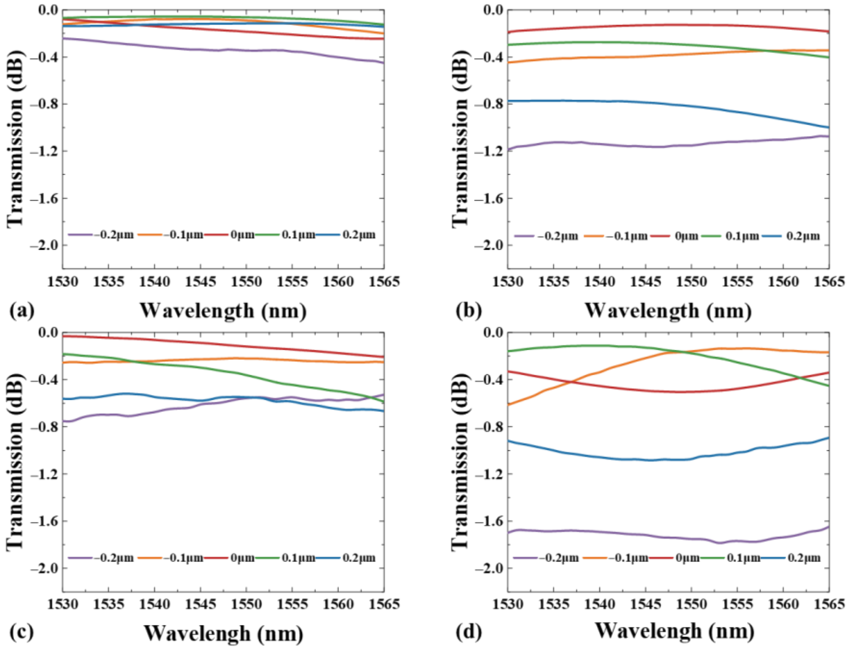

Figure 5. Simulated spectra with different fabricated errors for (**a**) E_{00} mode, (**b**) E_{10} mode, (**c**) E_{20} mode, (**d**) E_{30} mode.

3. Device Fabrication and Characterization

The device was fabricated on a six-inch silicon-dioxide wafer. First, a 20 μm thick silica lower cladding layer was grown on the silicon substrate via thermal oxidation. A 4 μm thick silicon dioxide core layer was then deposited onto the lower cladding layer using plasma-enhanced chemical vapor deposition (PECVD). Subsequently, the waveguide structure of the mode-selective switch was defined using inductively coupled plasma etching. A 20 μm thick silica upper cladding layer was deposited using PECVD. Finally, the electrodes were fabricated via magnetron sputtering and lift-off techniques. The footprint of the E_{00}/E_{10} mode-selective switch is approximately 1×30 mm^2, that of the E_{20}/E_{30} mode-selective switch is approximately 1×33 mm^2, and that of the E_{00}–E_{30} mode-selective switch is 1×60 mm^2. The fabricated four-stage cascaded adiabatic gradual broadband three-waveguide coupled mode-selective switch is shown in Figure 6a, which presents the photograph of the device after electrical packaging. Figure 6b–e show the optical microscope images of the waveguide structure. Figure 6f shows the SEM image of the waveguide cross-section.

To characterize the response time of the switch, a signal generator (SDG6032X-E, Siglent, Shenzhen, China) equipped with two probes is used as the driver. As illustrated in Figure 7a, the output optical signal is monitored using a high-speed photodetector connected to an oscilloscope (DS4024, RIGOL, Suzhou, China). The test system requires single-mode transmission. The device output end is designed with an asymmetric directional coupler structure for the E_{00}–E_{30} mode multiplexer/demultiplexer, which demultiplexes higher-order modes in a multimode bus into the fundamental mode. As shown in Figure 1e, this corresponds to the output ports labeled sequentially as O_j for the E_{00}–E_{30} modes (j = 1, 2, 3, 4). The mode demultiplexer design process and performance characterization have been introduced in our previous work [23]. The rise time (10–90%) of the switch is measured to be 0.86 ms, and the fall time (90–10%) is 0.64 ms. Both the

E_{00}/E_{10} and E_{20}/E_{30} mode-selective switches are tested; since they share the same platform materials, their response speeds are essentially identical. Additionally, the current–voltage (I–V) and optical power–voltage (O–V) characteristic curves of the switch are measured, shown in Figure 7b, yielding a resistance of 90.42 Ω. When a voltage of 4.8 V is applied to the upper modulation arm, the output mode is switched—this voltage corresponds to a power consumption of 266.22 mW to achieve a phase difference of π.

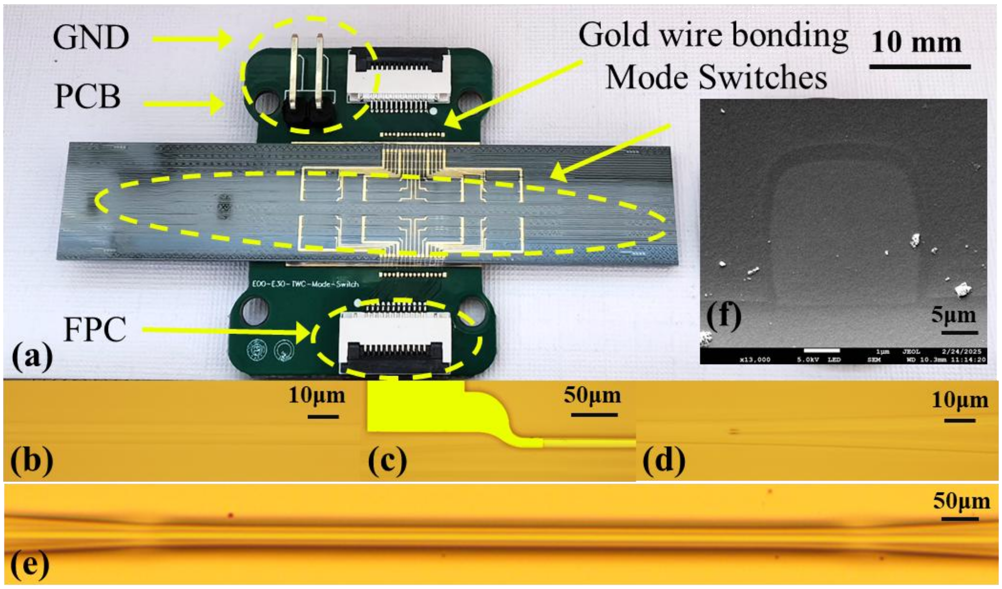

Figure 6. (**a**) Device after packaging; (**b**–**e**) local structure of the device under optical microscopy. (**f**) SEM image of the waveguide cross-section.

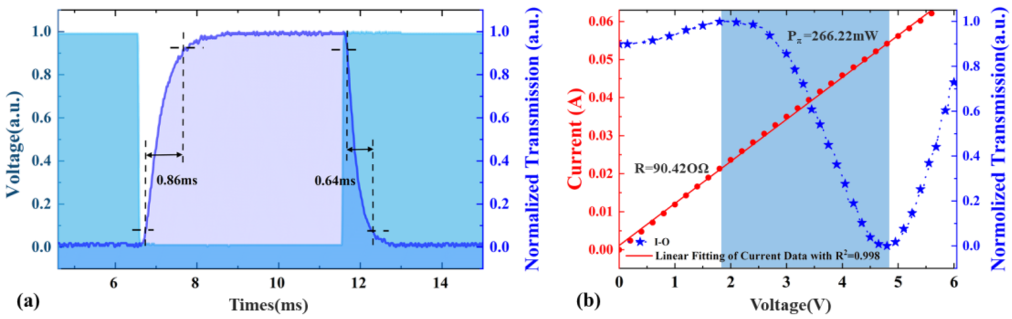

Figure 7. (**a**) Switch response time; (**b**) measured I-V (red curve) and O-V curves (blue curve) at 1550 nm.

A tunable laser (TSL-550, Santec, Komaki-City, Japan) is used as the light source. The TE-polarized fundamental mode is input into the device via end-face coupling, and the output light is then transmitted to an optical power meter (MPM200, Santec, Komaki-City, Japan) by using a single-mode fiber array (FA) for optical power detection.

The transmission spectra of mode MUX/DEMUX is shown in Figure 8. The performance of the device has undergone a red shift, resulting in poor CT between the E_{20} and E_{30} modes. The reference waveguide loss is lower than 7.1 dB at 1550 nm. Due to waveguide scattering loss scales with $(\Delta n)^3$ [24], the lower refractive index, and wide waveguide, the high-order modes can also show low transmission losses. We can calculate that at 1550 nm, the demultiplexer imposes an excess loss (EL) of 0.27 dB for the E_{00} mode, 0.78 dB for the E_{10} mode, 2.08 dB for the E_{20} mode, and 4.09 dB for the E_{30} mode. While this effectively reduces device size, the increased doping increases the flowability of the core material, leading to the melting of the core layer and the formation of undesirable waveguide shapes [25]. Furthermore, the emergence of an interdiffusion layer results in a broadening of the actual core layer range. As shown in Figure 6f, the core layer is 4.1 × 4.1 μm^2 without an interdiffusion layer (4.6 × 4.5 μm^2 with an interdiffusion layer). Through process optimization and an integrated layout design, the device's center wavelength can be aligned to 1550 nm.

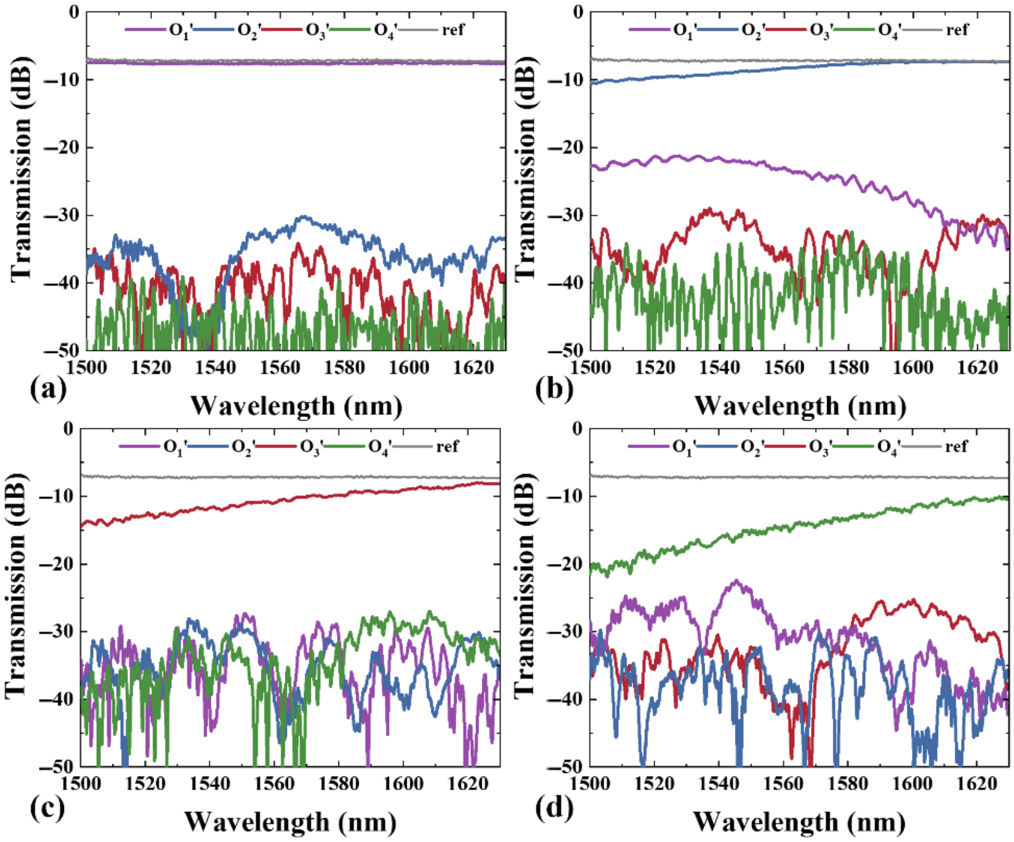

Figure 8. Transmission spectra of E_{00}–E_{30} Mode MUX/DEMUX: (**a**) $E_{00}-E_{00}-E_{00}$, (**b**) $E_{00}-E_{10}-E_{00}$, (**c**) $E_{00}-E_{20}-E_{00}$, (**d**) $E_{00}-E_{30}-E_{00}$.

The transmission spectrum of the E_{00}/E_{10} mode-selective switch is shown in Figures 9a and 10b. At 1550 nm, in the non-modulation state, IL is lower than 7.36 dB and CT is lower than −11.07 dB; in the electrode modulation state, the IL is lower than 7.86 dB and the CT is lower than −22.84 dB. The transmission spectrum of the E_{00}/E_{10} mode-selective switch is shown in Figures 9c and 10d. At 1550 nm, in the non-modulation state, IL is lower than 10.91 dB and CT is lower than −9.62 dB; in the electrode modulation state, the IL is lower than 10.75 dB and the CT is lower than −10.28 dB. With modulation, the EL of the E_{20}/E_{30} mode-selective switch is 1.11–3.47 dB. In the unmodulated state, the device exhibits a relatively high additional loss and poor CT. This is attributed to minor variations in the width of the modulation arm waveguide during fabrication, which introduce additional phase shifts. Consequently, the TWC position deviates from the ideal π phase difference, leading to performance degradation. Widening the modulation arm can mitigate process-induced effects and enhance device performance.

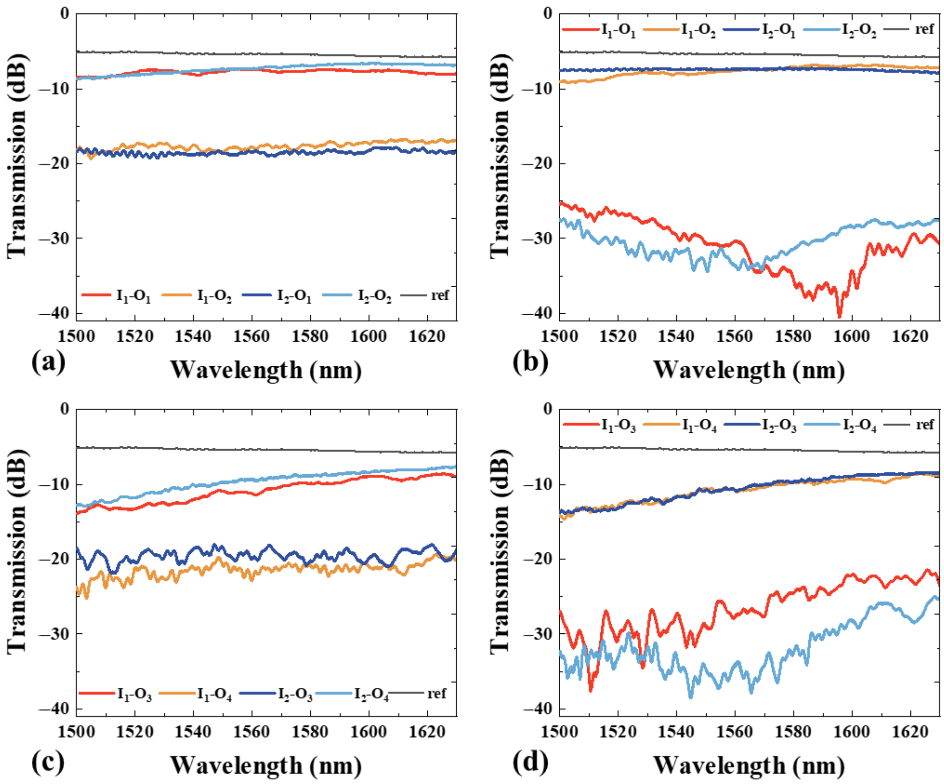

Figure 9. Transmission spectra of a cascaded 2-TWC mode-selective switch in the 1500–1630 nm wavelength range: (**a**) E_{00}/E_{10} mode device in non-modulation, (**b**) E_{00}/E_{10} mode device in modulation, (**c**) E_{20}/E_{30} mode device in non-modulation, (**d**) E_{20}/E_{30} mode device in modulation.

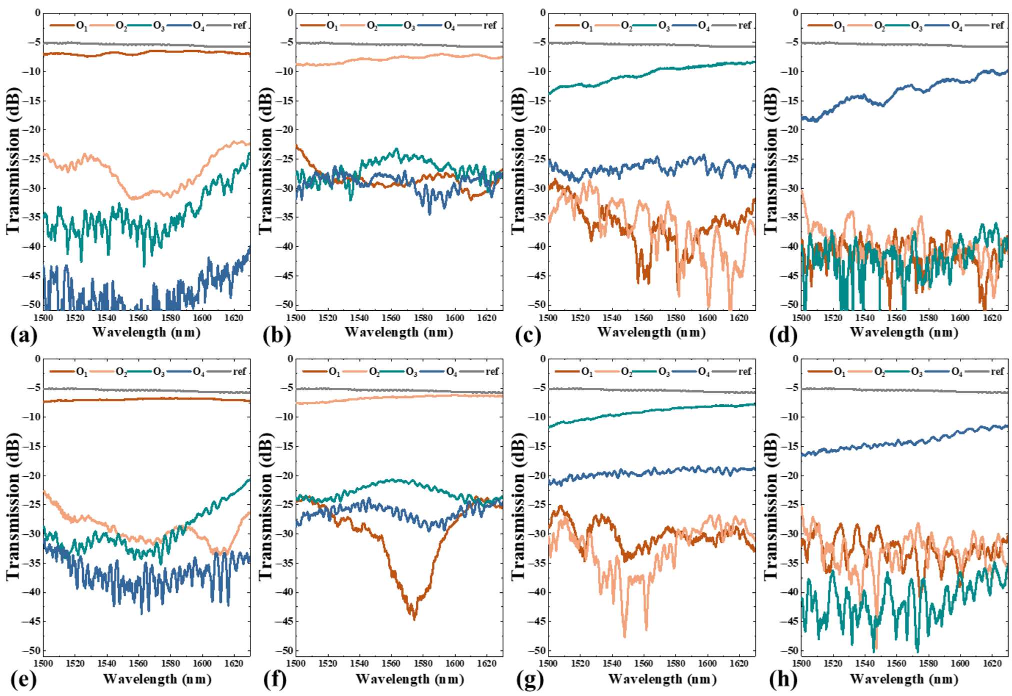

Figure 10. Transmission spectra of the E_{00}–E_{30} mode-selective switch. Through I_1: (**a**) in E_{00}-out E_{00} (**b**) in E_{00}-out E_{10} (**c**) in E_{00}-out E_{20} (**d**) in E_{00}-out E_{30}. Through I_2: (**e**) in E_{00}-out E_{00} (**f**) in E_{00}-out E_{10} (**g**) in E_{00}-out E_{20} (**h**) in E_{00}-out E_{30}.

4. E_{00}–E_{30} Mode-Selective Switch

The two-mode-selective switches are regarded as a basic component for advanced functions. To demonstrate their scalability and flexibility, two components are cascaded on a bus waveguide, with three electrodes added to control the phase difference between the two light beams. As shown in the structural schematic of Figure 1a, this configuration allows the selective output of any mode from E_{00} to E_{30}. A mode demultiplexer is connected to the output end. The device has two input ports (I_1, I_2) and four output ports (O_1–O_4).

The phase shifts generated by the three electrodes S_{1-3} is defined as $\Delta\varphi_\alpha$, $\Delta\varphi_\beta$, and $\Delta\varphi_\gamma$. By modulating these three groups of phase shifts in different combinations, the output of any mode of E_{00}~E_{30} can be realized. Taking the input E_{00} mode output E_{20} mode as an example, when the modulation conditions are set to $\Delta\varphi_\alpha = \pi$, $\Delta\varphi_\beta = \pi$, and $\Delta\varphi_\gamma = 0$, the signal light will be coupled to the E_{20} mode at $TWCR_3$ and enter the bus waveguide. The correspondence between the remaining different input ports (I_1/I_2), different phase shift combinations, and output modes can be referred to the electrode voltage parameters summarized in Table 2.

Table 2. Modulation voltages for different operating states of the E_{00}–E_{30} mode-selective switch.

	Input I_1				Input I_2			
S_1 ($\Delta\varphi_\alpha$)	0	5.1 V	5.1 V	5.1 V	5.1 V	0	0	0
S_2 ($\Delta\varphi_\beta$)	0	0	4.9 V	4.9 V	0	0	4.7 V	4.7 V
S_3 ($\Delta\varphi_\gamma$)	0	0	0	5.5 V	0	0	0	4.5 V
Output mode	E_{00}	E_{10}	E_{20}	E_{30}	E_{00}	E_{10}	E_{20}	E_{30}
Output port	O_1	O_2	O_3	O_4	O_1	O_2	O_3	O_4

To contextualize the previously reported IL and CT values derived from transmission spectra, at 1550 nm, the loss of a reference straight waveguide was tested and plotted as a dashed line in the figures. Figure 10a–d show the device's transmission spectra, where when the E_{00} mode is input from port I_1, the IL and CT values are 6.92 dB and −23 dB for E_{00} output, 7.96 dB and −16.79 dB for E_{10} output, 10.83 dB and −12.8 dB for E_{20} output, and 15.56 dB and −14.8 dB for E_{30} output. Figure 10e–h present the transmission spectra for the E_{00} mode input from port I_2, corresponding to IL and CT values of 7.00 dB and −23.03 dB for E_{00} output, 6.62 dB and −14.96 dB for E_{10} output, 9.36 dB and −10.57 dB for E_{20} output, and 14.69 dB, and −15.91 dB for E_{30} output. With modulation, the EL of the E_{00}–E_{30} mode-selective switch is 1.28–6.12 dB.

The measurement results experimentally demonstrate that both the designed unit structure and the cascaded architecture can effectively achieve mode-selective output. This finding highlights the scalability and flexibility of the proposed approach, as well as its potential for enabling more advanced functionalities in related systems.

The mode demultiplexer is the main factor affecting the high-order mode IL in device test data, as shown in Figure 8. Through process optimization and integrated layout design, the device's center wavelength can be aligned to 1550 nm. By employing a fully automatic phase error calibration technique, this method dynamically compensates for phase errors. This significantly improves the precision and efficiency of the calibration process amid process-induced variations [26]. The loss of the mode demultiplexer also can be reduced by using a conical ADC structure [27,28]. The power consumption can be further reduced through the structure of air isolation slots [29]. The response speed can be reduced by reducing the thickness of the top cladding layer. The mode switch designed in this paper has the advantages of low transmission loss and a high mode extinction ratio, hence it has broad application prospects in MDM systems.

5. Discussion

The comparisons of performance metrics for different mode switches are shown in Table 3. Refs. [14,19,30] implemented mode conversion via electro-optic modulation on TFLN and SOI platforms. Electro-optic switches offer fast response speeds and generally consume less power than thermo-optic switches; however, bias point drift during long-term operation compromises their robustness compared with thermo-optic switches. Moreover, the shorter modulation arms in thermo-optic switches allow for a more compact device structure. Ref. [31] demonstrated mode switching on a polymer platform. Benefiting from the high thermo-optic coefficient of polymers, a high extinction ratio can be achieved with a low power consumption. Nevertheless, the robustness of polymer platforms remains challenging, and their non-CMOS compatibility poses obstacles for commercialization. Ref. [32] is our previous work. Based on this work, we expanded the device structure by introducing a TWC scheme alongside adiabatic directional coupler coupling, which enhanced the structural functionality of the device. In our work, we exhibit an E_{00}/E_{10} mode switch and an E_{20}/E_{30} mode switch at 1550 nm with IL of 7.86 dB and 10.76 dB, respectively. The ELs are 1.73 dB and 3.46 dB which is closer to the reported values. The devices show better CT. We also exhibit the non-crossing E_{00}–E_{30} mode switch with IL of 15.56 dB and CT of −10.57 dB. By optimizing the TWCs and mode demultiplexers for E_{20} and E_{30}, the device can achieve a lower additional loss. By introducing the isolation trenches [18,33], the power consumption and footprint can be reduced.

Table 3. Comparison of performance metrics for different mode switches.

Ref.	Modes	Platform	IL (dB)	ER (dB)	CT (dB)	Speed (ms)	Bandwidth (nm)
[30]	E_{00} & E_{10}	TFLN	14.5	18.7	−16.9	23/30 ns	1530–1565
[19]	E_{00} & E_{10}	SOI	2.8 [a]	N.A.	−13.7	N.A.	1525–1565
[14]	E_{00}–E_{30}	SOI	2.1 [a]	N.A.	−19.7	N.A.	1525–1565
[31]	E_{11} & E_{21}	Polymer	11.3	17.5/16.4	N.A.	~1.3	1530–1565
[32]	E_{00} & E_{10}	Silica	4.56	17	−24.27	0.56/0.79	1500–1600
This work	E_{00} & E_{10}	Silica	7.86	22.84	−23.66	0.86/0.64	1500–1630
	E_{20} & E_{30}	Silica	10.76	18.28	−18.28	0.86/0.56	1500–1630
	E_{00}–E_{30}	Silica	15.56	N.A.	10.57	N.A.	1500–1630

[a] Excess loss. N.A.: Not Available.

6. Conclusions

In conclusion, we propose and demonstrate a broadband three-waveguide coupled mode switch based on adiabatic progression. As a proof of concept, we first design two cascaded mode-selective switches, namely the E_{00}/E_{10} mode-selective switch and the E_{20}/E_{30} mode-selective switch. The rise time (10–90%) of the optical signal is 0.86 ms, the fall time (90–10%) is 0.64 ms, and the modulation power consumption is 266.22 mW. Dynamic response spectra in the wavelength range of 1500–1630 nm show that the inter-mode CT of the E_{00}/E_{10} (E_{20}/E_{30}) mode-selective switch is lower than −16.23 dB (−14.97 dB). Furthermore, we realize a four-mode (E_{00}–E_{30}) selective switch by cascading four TWCs through a bus waveguide; when optical signals are input from I_1 and I_2, respectively, the inter-mode CT is lower than −15.56 dB and −10.57 dB, at 1550 nm. This device exhibits excellent scalability and flexibility and holds great application potential in increasingly complex and flexible MDM systems.

Author Contributions: Conceptualization, M.Z., Y.D. and G.Z.; methodology, D.Z., M.Z., Y.D. and G.Z.; software, M.Z., S.Z. and Y.D.; validation, M.Z.; formal analysis, M.Z., S.Z. and D.Z.; investigation, M.Z.; resources, D.Z.; data curation, M.Z. and S.Z.; writing—original draft preparation, M.Z. and Y.D.; writing—review and editing, M.Z., S.Z. and G.Z.; visualization, M.Z., S.Z. and G.Z.; supervision, D.Z.; project administration, D.Z.; funding acquisition, D.Z. All authors have read and agreed to the published version of the manuscript.

Funding: This research was funded by the National Natural Science Foundation of China (No. 62475091) and the Jilin University Pilot-Scale Selection Program (No. 24GNYZ13).

Institutional Review Board Statement: Not applicable.

Informed Consent Statement: Not applicable.

Data Availability Statement: The original contributions presented in the study are included in the article; further inquiries can be directed to the corresponding author.

Acknowledgments: Thanks to Yuexin Yin from Jilin University for providing valuable advice and technical support in the design and testing of the devices, and thanks to Shijia Company for their assistance in the device's fabrication.

Conflicts of Interest: The authors declare no conflicts of interest.

Abbreviations

The following abbreviations are used in this manuscript:

TWC	Three-waveguide coupling
MDM	Mode division multiplexing
IL	Insertion loss
CT	Crosstalk
TWCR	Three-waveguide coupling region
WG	Waveguide
PECVD	Plasma-enhanced chemical vapor deposition
BPM	Beam propagation method

References

1. Saha, N.; Brunetti, G.; Armenise, M.N.; Ciminelli, C. Tunable narrow band add-drop filter design based on apodized long period waveguide grating assisted co-directional coupler. *Opt. Express* **2022**, *30*, 28632. [CrossRef] [PubMed]
2. Wang, M.; Zhang, X.; Xin, Y.; Liu, T.; Fang, J.; Sun, X.; Wu, Y.; Zhang, D. Novel silica waveguide-type polarization beam splitters based on MMI coupler with extraordinary gratings. *IEEE Electron. Device Lett.* **2025**, *46*, 1461–1464. [CrossRef]
3. Yuan, M.; Zhou, X.; Jiang, Y.; Ma, X.; Xiao, H.; Low, M.X.; Dubey, A.; Nguyen, T.G.; Ren, G.; Mitchell, A.; et al. Meta-Waveguides for Scalable and Robust Optical Mode Manipulation on Etchless Thin Film Lithium Niobate. *ACS Photonics* **2025**, *12*, 5271–5282. [CrossRef]
4. Shuhrawardy, M.; Ahmmed, K.T.; Yeung, C.H.; Jin, W.; He, L.; Li, B.; Chan, H.P. Reconfigurable Three-Mode Converter for Flexible Mode Division Multiplexing Optical Networks. *IEEE Photonics J.* **2024**, *16*, 6601009. [CrossRef]
5. Han, X.; Xiao, H.; Jiang, Y.; Ren, G.; Zhang, P.; Tan, J.; Yang, J.; Mitchell, A.; Tian, Y. Integrated non-blocking optical router harnessing wavelength- and mode-selective property for photonic networks-on-chip. *Opt. Express* **2021**, *29*, 1251. [CrossRef]
6. Tian, Y.; Li, J.; Wu, Z.; Chen, Y.; Zhu, P.; Tang, R.; Mo, Q.; He, Y.; Chen, Z. Wavelength-interleaved MDM-WDM transmission over weakly-coupled FMF. *Opt. Express* **2017**, *25*, 16603. [CrossRef]
7. Jiang, W.; Mao, S.; Hu, J. Inverse-designed counter-tapered coupler based broadband and compact silicon mode multiplexer/demultiplexer. *Opt. Express* **2023**, *31*, 33253. [CrossRef]
8. He, Y.; Li, X.; Zhang, Y.; An, S.; Wang, H.; Wang, Z.; Chen, H.; Huang, Y.; Huang, H.; Fontaine, N.K.; et al. On-chip metamaterial-enabled high-order mode-division multiplexing. *Adv. Photonics* **2023**, *5*, 056008. [CrossRef]
9. Cheng, C.; Yang, S.; Liu, W.; Liu, S.; Huo, Y.; Fu, X.; Yang, L. Ultra-Compact Inverse Designed Multimode Waveguide Bend Based on Levelset Method. *IEEE Photonics Technol. Lett.* **2024**, *36*, 571–574. [CrossRef]
10. Kawaguchi, Y.; Tsutsumi, K. Mode multiplexing and demultiplexing devices using multimode interference couplers. *Electron. Lett.* **2002**, *38*, 1701–1702. [CrossRef]
11. Lee, B.-T.; Shin, S.-Y. Mode-order converter in a multimode waveguide. *Opt. Lett.* **2003**, *28*, 1660–1662. [CrossRef]
12. Bagheri, S.; Green, W.M. Silicon-on-insulator mode-selective add-drop unit for on-chip mode-division multiplexing. In *Proceedings of the 2009 6th IEEE International Conference on Group IV Photonics, San Francisco, CA, USA, 9–11 September 2009*; IEEE: New York, NY, USA, 2009; pp. 166–168.
13. Ding, Y.; Xu, J.; Da Ros, F.; Huang, B.; Ou, H.; Peucheret, C. On-chip two-mode division multiplexing using tapered directional coupler-based mode multiplexer and demultiplexer. *Opt. Express* **2013**, *21*, 10376–10382. [CrossRef]
14. Jia, H.; Fu, X.; Zhou, T.; Zhang, L.; Yang, S.; Yang, L. Mode-selective modulation by silicon microring resonators and mode multiplexers for on-chip optical interconnect. *Opt. Express* **2019**, *27*, 2915. [CrossRef]
15. Liu, Z.; Xia, F.; Yan, R.; Wang, P.; Jiang, Y. Multi-dimensional reconfigurable optical add/drop multiplexer for WDM-MDM systems. *Opt. Express* **2025**, *33*, 15532. [CrossRef] [PubMed]

16. Liu, W. Flexible on-chip mode-division switching with a new mode converter design. *arXiv* **2017**, arXiv:1712.01658.
17. Shen, W.; Du, J.; Xu, K.; He, Z. On-Chip Selective Dual-Mode Switch for 2-μm Wavelength High-Speed Optical Interconnection. *IEEE Photonics Technol. Lett.* **2021**, *33*, 483–486. [CrossRef]
18. Jiang, Y.; Han, X.; Li, Y.; Xiao, H.; Huang, H.; Zhang, P.; Dubey, A.; Yuan, M.; Nguyen, T.G.; Boes, A.; et al. High-Speed Optical Mode Switch in Lithium Niobate on Insulator. *ACS Photonics* **2023**, *10*, 2257–2263. [CrossRef]
19. Xiao, H.; Liu, Z.; Han, X.; Yang, J.; Ren, G.; Mitchell, A.; Tian, Y. On-chip reconfigurable and scalable optical mode multiplexer/demultiplexer based on three-waveguide-coupling structure. *Opt. Express* **2018**, *26*, 22366. [CrossRef] [PubMed]
20. Yin, Y.-X.; Zhang, X.-P.; Yin, X.-J.; Li, Y.; Xu, X.-R.; An, J.-M.; Wu, Y.-D.; Liu, X.-P.; Zhang, D.-M. High-Q-Factor Tunable Silica-Based Microring Resonators. *Photonics* **2021**, *8*, 256. [CrossRef]
21. Wang, M.; Xin, Y.; Yao, Z.; Liu, T.; Fang, J.; Sun, X.; Wu, Y.; Zhang, D. Compact Broadband Edge Coupler Based on Trident Gratings for Silica Platform. *IEEE Photonics Technol. Lett.* **2025**, *37*, 227–230. [CrossRef]
22. Watanabe, K.; Hashizume, Y.; Nasu, Y.; Kohtoku, M.; Itoh, M.; Inoue, Y. Ultralow Power Consumption Silica-Based PLC-VOA/Switches. *J. Light. Technol.* **2008**, *26*, 2235–2244. [CrossRef]
23. Mao, D.; Wang, Y.; Xu, L.; El-Fiky, E.; Jacques, M.; Zhang, J.; Alam, M.S.; Kumar, A.; D'Mello, Y.; Plant, D.V. Adiabatic coupler with nonlinearly tapered mode-evolution region. *IEEE Photonics Technol. Lett.* **2021**, *33*, 840–843. [CrossRef]
24. Hong, S.; Zhang, L.; Wang, Y.; Zhang, M.; Xie, Y.; Dai, D. Ultralow-loss compact silicon photonic waveguide spirals and delay lines. *Photonics Res.* **2022**, *10*, 1–7. [CrossRef]
25. Ma, J.; Wang, L.; Sun, B.; Chen, J.; Zhang, J.; Wang, Y.; An, J.; Wu, Y. High-Performance Compact 48-Channel Arrayed Waveguide Grating on Improved Silica Platform. *Microw. Opt. Technol. Lett.* **2025**, *67*, e70090. [CrossRef]
26. Song, L.; Jiao, X.; Cao, Z.; Liu, W.; Zou, S.; Fang, X.; Fan, S.; Li, H.; Shi, Y.; Dai, D. Scalability of Ultralow-Loss Calibration-Free Silicon Photonic Mach-Zehnder Switches. *Laser Photonics Rev.* **2025**, *19*, 2401353. [CrossRef]
27. Zheng, S.; Huang, M.; Cao, X.; Wang, L.; Ruan, Z.; Shen, L.; Wang, J. Silicon-based four-mode division multiplexing for chip-scale optical data transmission in the 2 μm waveband. *Photonics Res.* **2019**, *7*, 1030–1035. [CrossRef]
28. Chen, W.; Li, H.; Zhang, B.; Wang, P.; Dai, S.; Liu, Y.; Li, J.; Li, Y.; Fu, Q.; Dai, T.; et al. Silicon Mode (de)Multiplexer Based on Cascaded Particle-Swarm-Optimized Counter-Tapered Couplers. *IEEE Photonics J.* **2021**, *13*, 6600210. [CrossRef]
29. Niu, D.; Sun, S.; Xu, Q.; Jiang, M.; Wang, X.; Li, Z.; Chen, C.; Wu, Y.; Zhang, D. Optimized design and fabrication of polymer/silica thermo-optic switch with low power consumption. *Appl. Opt.* **2017**, *56*, 5799–5803. [CrossRef] [PubMed]
30. Zhang, M.; Chen, K.; Wang, M.; Wu, J.; Chiang, K.S. Electro-optic reconfigurable two-mode (de)multiplexer on thin-film lithium niobate. *Opt. Lett.* **2021**, *46*, 1001. [CrossRef]
31. Lin, B.; Sun, S.; Sun, X.; Lian, T.; Zhu, M.; Che, Y.; Wang, X.; Zhang, D. Dual-Mode 2×2 Thermo-Optic Switch Based on Polymer Waveguide Mach-Zehnder Interferometer. *IEEE Photonics Technol. Lett.* **2022**, *34*, 1317–1320. [CrossRef]
32. Ding, Y.; Yin, Y.; Guan, B.; Xu, Z.; Yin, X.; Wu, Y.; Sun, X.; Zhang, D. Mode-selective switch on silica-based PLC platform. *Opt. Commun.* **2023**, *546*, 129757. [CrossRef]
33. Zhang, Z.; Skandalos, I.; Ma, R.; Chen, M.; Sun, B.; Zhong, C.; Gardes, F.; Cheng, Q.; Penty, R. Compact deep-groove-assisted bends on SiN platform for monolithic integrated laser. *Opt. Express* **2025**, *33*, 4383–4395. [CrossRef] [PubMed]